aerospace

MDPI

Article

Noise Prediction and Plasma-Based Control of Cavity Flows at a High Mach Number

Hongming Cai [1,*], Zhuoran Zhang [1], Ziqi Li [2] and Hongda Li [3]

[1] Academy of Astronautics, Nanjing University of Aeronautics and Astronautics, Nanjing 210016, China; zhangzhuoran@nuaa.edu.cn
[2] Aircraft Design Institute, Jiangxi Hongdu Aviation Industry Co., Ltd., Nanchang 330095, China; songnifeixiang650@163.com
[3] School of Aeronuatica Engineering, Nanjing Vocational University of Industry Technology, Nanjing 210023, China; 2021101181@niit.edu.cn
* Correspondence: caihongming@nuaa.edu.cn

Abstract: Cavity flows are a prevalent phenomenon in aerospace engineering, known for their intricate structures and substantial pressure fluctuations arising from interactions among vortices. The primary objective of this research is to predict noise levels in high-speed cavity flows at Mach 4 for a rectangular cavity characterized by an aspect ratio of L/D = 7. Moreover, this study delves into the influence of the plasma actuator on noise control within the cavity flow regime. To comprehensively analyze acoustic characteristics and explore effective noise reduction strategies, a computational fluid dynamics technique with the combination of a delayed detached eddy simulation (DDES) and plasma phenomenological model is established. Remarkably, the calculated overall sound pressure level (OASPL) and plasma-induced velocity closely align with the experimental data, validating the reliability of the proposed approach. The results show that the dielectric barrier discharge (DBD) plasma actuator changes the movement range of a dominating vortex in the cavity to affect the OASPL at the point with the maximum noise level. The control of excitation voltage can reduce the cavity noise by 2.27 dB at most, while control of the excitation frequency can only reduce the cavity noise by 0.336 dB at most. Additionally, the increase in excitation frequency may result in high-frequency sound pressure, but the influence is weakened with the increase in the excitation frequency. The findings highlight the potential of the plasma actuator in reducing high-Mach-number cavity noise.

Keywords: cavity flows; noise prediction; flow control; delayed detached eddy

check for updates

Citation: Cai, H.; Zhang, Z.; Li, Z.; Li, H. Noise Prediction and Plasma-Based Control of Cavity Flows at a High Mach Number. *Aerospace* **2023**, *10*, 922. https://doi.org/10.3390/aerospace10110922

Academic Editor: Konstantinos Kontis

Received: 6 September 2023
Revised: 25 October 2023
Accepted: 25 October 2023
Published: 29 October 2023

1. Introduction

Cavity structures find extensive application in advanced aircraft and propulsion systems, such as internal weapon bays and landing gear bays of aircraft [1]. On one hand, cavity structures play a proactive role in enhancing stealth performance and reducing the aerodynamic drag during aircraft cruising. On the other hand, cavity structures also introduce aerodynamic noise-related challenges [2–4], which could potentially lead to structural fatigue or electronic equipment damage within weapon bays, posing a significant impact on flight safety. Research indicates that the generation of cavity noise is closely linked to unsteady flow patterns and complex wave systems within the cavity. Under specific conditions, cavity flows are prone to undergo flow–acoustic coupling phenomena, resulting in distinct periodic pressure oscillations and producing high-amplitude pure-tone noise [5].

In recent years, there has been in-depth experimental research into the spatiotemporal evolution process of complex wave systems in supersonic cavities, leading to the formulation of corresponding mechanistic models [6,7]. Ryan F. Schmit et al. [8] investigated the flow physics phenomena within cavities using wind tunnel experiments. Taro

Handa et al. [9] explored the relationship between shear layer motion, pressure wave generation, and cavity trailing edge pressure oscillations through wind tunnel experiments. N. T. Clemens et al. [10] conducted wind tunnel experiments to explore the physical foundation of oscillation periods in high-Mach-number, turbulent, open cavity flows.

In the simulation regime, Rizzetta et al. [11] employed large eddy simulation techniques to investigate the noise feedback mechanism in closed cavities. Kyoung Sik Chang et al. [12] employed Reynolds-averaged Navier–Stokes/large eddy simulation (RANS/LES) methods to study the acoustic characteristics of deep cavities. Shia-Hui Peng et al. [13] conducted cavity flow analysis using DES and a hybrid RANS/LES approach, achieving favorable results. Hamed et al. [14] employed an SST-based DES method to compute pressure fluctuations in a Ma = 1.19 cavity and compared the results with the experimental data. Yin Tang et al. [15] utilized IDDES to study flow control methods for acoustic characteristics of open cavities at Ma = 3.51. Xuhong Jin et al. [16] employed direct simulation Monte Carlo methods to investigate the impact of inlet boundary layer thickness on cavity flow characteristics. Larsson J et al. [17] directly solved the compressible Navier–Stokes equations to study laminar flow and near-field acoustics in a two-dimensional open cavity at Ma = 0.15. S. J. Lawson et al. [18] conducted DES-based research on the geometries of the M219 experimental cavity and the 1303 uninhabited combat air vehicle cavity geometry.

Although a series of experimental and numerical studies have been conducted on the unsteady flow characteristics of cavities, most of the research has focused on cavities with Ma < 2. As aircraft move towards higher speeds and longer distances, the engineering applications of high-Mach-number (Ma > 2) cavities have become more prominent. Research on high-Mach-number (Ma > 2) cavity flows is relatively limited and further studies are warranted.

Noise is the byproduct of high-Mach-number cavity flows, and the advancement in understanding the mechanisms behind cavity noise generation has spurred the development of noise control techniques. In recent years, a variety of supersonic cavity noise control methods have been devised. Zhang et al. [19] proposed a control method that modifies the shape of the cavity leading-edge surface to increase the leading-edge height. Zhuang [20] employed the approach of microjets at the leading edge to modify the incoming Mach number, thereby reducing aerodynamic noise within the cavity. Vakili and Gauthier [21] utilized leading-edge jets to alter the cavity's inlet boundary layer thickness and consequently reduce cavity noise.

Luo et al. [22] conducted numerical simulations of the M219 cavity flow at Ma = 1.5 using different serrated leading-edge sawtooth spoilers. Alam et al. [23] achieved pressure oscillation control within the cavity flow by utilizing a sub-cavity at the leading edge. Schmit et al. [24] experimentally studied supersonic cavity flow using leading-edge vortex generators. Danilov et al. [25] achieved noise reduction by perturbing the cavity shear layer using vortex generators. Thangamani et al. [26] investigated cavity noise control through modifications at the trailing edge. Vikramaditya et al. [27] explored the influence of different rear-wall inclination angles on the cavity's internal noise characteristics.

Despite these studies, there remains a notable research gap in the field of noise control for high-Mach-number cavity flows, necessitating further investigation and exploration. As such, there is an evident need to bridge this gap in knowledge and advance our understanding of noise generation and control mechanisms within high-Mach-number cavity flows. This study endeavors to contribute to filling this void by comprehensively exploring the complexities of noise generation and developing effective noise control strategies within the context of high-Mach-number cavity flows.

This paper is organized as follows: Section 2 establishes the numerical methods used for analysis, encompassing a comprehensive literature review and methodology overview. Validation of these methods follows in Section 3 through rigorous experimental and numerical verification. Section 4 delves into the heart of the study, presenting detailed analyses of noise characteristics, flow structures, and the intricate interplay within high-Mach-number cavity flows. Parameters such as excitation voltage and frequency are systematically investigated to elucidate their impact on noise generation and propagation. Finally, Section 5 synthesizes our findings into insightful conclusions, discussing both the fundamental understanding gained and the practical implications for noise control in high-Mach-number cavity flows. This structured approach not only advances our understanding of noise mechanisms but also provides a roadmap for addressing cavity noise challenges in high-Mach-number environments.

2. Numerical Simulation Methods

2.1. Flow Simulation Method

The numerical investigation of the intricate characteristics of high-Mach-number cavity flows requires an appropriate computational method. In this section, we established a DDES-based method to capture the complex flow structure and acoustic characteristics. The detached eddy simulation (DES) [28] technique emerges as a compelling approach to simulate cavity flows due to its inherent capability to bridge the gap between the Reynolds-averaged Navier–Stokes (RANS) [29] and large eddy simulation (LES) [30] methods. This coupling algorithm offers a refined way of resolving the intricate flow structures present in cavity flows, ranging from the near-wall boundary layer to the regions experiencing significant flow separation.

Extending the foundational framework of DES, the DDES method introduces a novel refinement—the integration of a delay function. This function serves as a sophisticated criterion for transitioning between RANS and LES modes based on the local flow characteristics. By incorporating this delay function, the DDES method enhances the accuracy and fidelity of the simulation by seamlessly blending the strengths of both RANS and LES, while effectively mitigating their respective limitations.

Building upon the DES framework, the DDES [31] method introduces a delay function to modify the criteria for transitioning between RANS and LES modes accordingly:

$$\widetilde{d} = d - f_d \max(0, d - C_{des} L_g) \tag{1}$$

where the delay function f_d is defined as

$$f_d = 1 - \tanh\left[(8r_d)^3\right] \tag{2}$$

$$r_d = \frac{v_T + v}{\sqrt{U_{i,j}U_{i,j}}\kappa^2 d^2} \tag{3}$$

In the equation, C_{des} is the adaptive parameter, L_g is the grid scale, v_T is the viscosity of vortex motion, v is the viscosity coefficient of molecular motion, $U_{i,j}$ is the velocity gradient, κ is the Karman length, and d is the distance from the object surface. r_d represents the ratio of turbulent scale at a given location to the distance from that location to the wall. This parameter ensures that LES is not used within the boundary layer, and the DDES model transitions to the LES mode in regions of pronounced separation. In areas farther from the wall where $r_d << 1$ and $f_d = 1$, LES is utilized, while RANS is employed in other regions where $f_d = 0$.

2.2. Plasma Actuator Model

This section introduces an employed phenomenological model [32] and showcases its significance in capturing the effects of plasma actuation on cavity flows. Through this approach, we aim to elucidate the intricate mechanisms of plasma-induced flow control. Plasma actuation stands as a promising avenue for actively manipulating the flow characteristics within cavities. The pivotal concept underpinning this model revolves around the direct integration of experimental and theoretical findings into the computational framework. Specifically, the range and distribution of electric field forces, gleaned from meticulous experiments and theoretical analyses, are seamlessly incorporated as source terms within the computational equations.

The integration of plasma-induced effects directly into the computational framework introduces a dynamic and interactive component to the simulation. This empowers us to effectively emulate the intricate interplay between plasma actuation and the surrounding flow field. By intertwining the electric field forces with the governing equations, we gain a holistic perspective on how plasma actuation influences the flow's behavior, leading to alterations in vortical structures, pressure distributions, and, ultimately, acoustic signatures.

A simplification of the plasma interaction region, represented as a right-angled triangle OAB with width b and height a, is depicted in Figure 1. Within this region, the electric field forces exhibit a linear distribution, attaining maximum strength E_0 at the origin O and breakdown electric field strengths E_b along the OA, OB, and AB edges. When the electric field strength E_b falls below the truncated electric field strength, the electric field forces are insufficient to penetrate the gas, thereby inhibiting plasma formation, and, thus, their influence can be disregarded. Throughout the triangular region, the electric field forces align parallel to the AB edge.

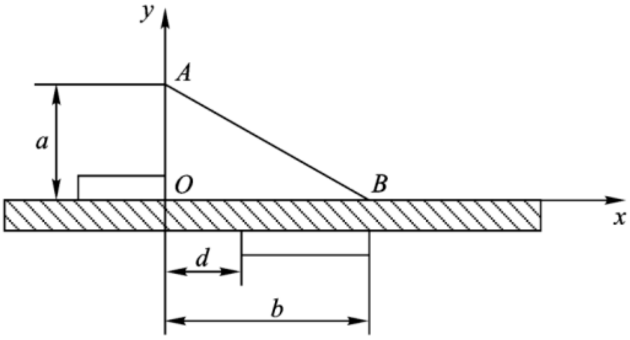

Figure 1. Schematic of plasma actuator and volume-force acting region.

The phenomenological model efficiently encapsulates the influence of the plasma excitation region on the flow field by incorporating the electric field forces. The resulting simulation outcomes will be critically assessed against the experimental data to validate the efficacy of the proposed plasma actuator model.

The electric field strength can be described by the following equations:

$$|E| = E_0 - k_1 x - k_2 y \tag{4}$$

$$k_1 = \frac{E_0 - E_b}{b}, k_2 = \frac{E_0 - E_b}{a} \tag{5}$$

where E_0 is the electric field strength at point O, representing the maximum electric field strength; the electric field strength at the AB boundary (denoted as E_b) corresponds to the breakdown electric field strength. If the electric field strength falls below this value, the effect of the electric field forces is neglected.

The electric field force is oriented parallel to the hypotenuse AB of the triangle. This leads to the magnitudes of the electric field strengths in the x and y directions, which are defined by:

$$E_x = \frac{Ek_2}{\sqrt{k_1^2 + k_2^2}}, E_y = \frac{Ek_1}{\sqrt{k_1^2 + k_2^2}} \tag{6}$$

According to the phenomenological simulation model proposed in reference [33], the volume forces in the x and y directions within the plasma interaction region are defined by:

$$\begin{cases} F_{tavex} = v\alpha\rho_c e_c E_x \Delta t \delta \\ F_{tavey} = v\alpha\rho_c e_c E_y \Delta t \delta \end{cases} \tag{7}$$

where v represents frequency. α denotes the effective coefficient for elastic collisions. ρ_c stands for charge density. e_c signifies the elementary charge constant. Δt signifies the discharge time. δ represents the Dirac delta function, utilized to delineate the extent of the electric field force. When $E \geq E_b$, its effect is accounted for as δ = 1; otherwise, it is treated as 0.

3. Validation of the Established Method

3.1. Validation of DDES Approach

To assess the reliability and accuracy of the DDES approach, we embark on a rigorous validation exercise utilizing a standard high-Mach-number cavity case with the experimental data. This benchmark case serves as a touchstone, allowing us to ascertain the ability of the DDES method to replicate known acoustic characteristics. In the subsequent section, we will present and discuss the outcomes of our DDES simulations on the standard cavity case.

The validation case utilized the standard cavity benchmark from reference [34]. The cavity model has a length (L) of 0.4572 m, and a width (W) and depth (D) of 0.1016 m each, resulting in an aspect ratio of 4.5:1. Computational parameters in this study match the experimental conditions to ensure the feasibility and accuracy of the numerical simulation. Specifically, the following parameters are used: incoming flow Mach number of 3.51, zero angle of attack, incoming static pressure of 2495.56 Pa, incoming static temperature of 93.08 K, and a Reynolds number based on the cavity length of 9.9×10^9. A structured grid is employed, with a finer mesh within the cavity to capture small-scale vortex structures, and a coarser mesh in the far-field region to expedite computations. The total number of grid cells is approximately 13 million (as shown in Figure 2). The SST-based DDES method is employed for unsteady turbulent calculations. The Roe flux-difference splitting (Roe-FDS) scheme is employed for flux splitting, with a second-order upwind scheme used for convective fluxes and a second-order central difference scheme for viscous diffusion terms. A second-order implicit dual-time-stepping scheme is adopted for time integration. The physical time step is set to 2×10^{-5} s, and a total of 2000 physical time steps are computed (corresponding to a total physical time of 0.04 s). The monitoring point corresponds to the pressure measurement location K18, as defined in reference [34]. The K18 point is located on the rear wall of the cavity, x/L = 1, y/L = 0, z/L = −0.1706, as shown in Figure 3.

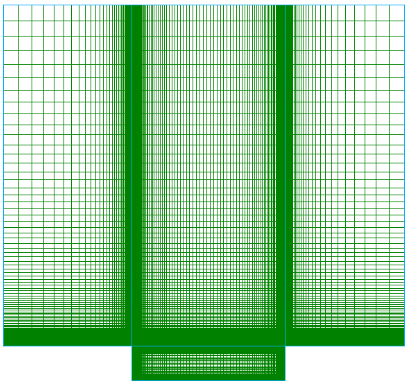

Figure 2. Computational grid of the cavity model.

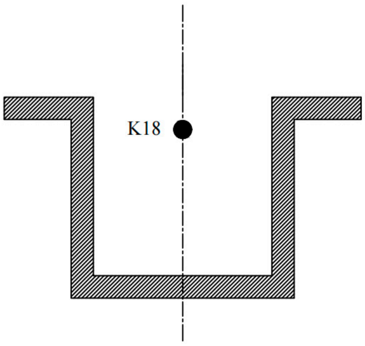

Figure 3. x/L = 1. Cross-sectional view.

Figure 4 illustrates the comparison between experimental and simulation results at monitoring point 18, while Table 1 provides the frequencies and sound pressure level amplitudes corresponding to dominant modes at monitoring point K18. The computed overall sound pressure level (OASPL) is 155.05 dB, whereas the experimental counterpart stands at 151.94 dB, yielding a discrepancy of 3.08 dB. The first-order mode shows a frequency error of 21.9% with a relative error in SPL of 4.08%. The second-order mode has a frequency error of 10.3% and a relative SPL error of 10.1%. The third-order mode indicates an error of 3.1% in frequency and a 3.2% relative error in SPL. The fourth-order mode displays a discrepancy of 3.97% in frequency and a 1.07% relative error in SPL.

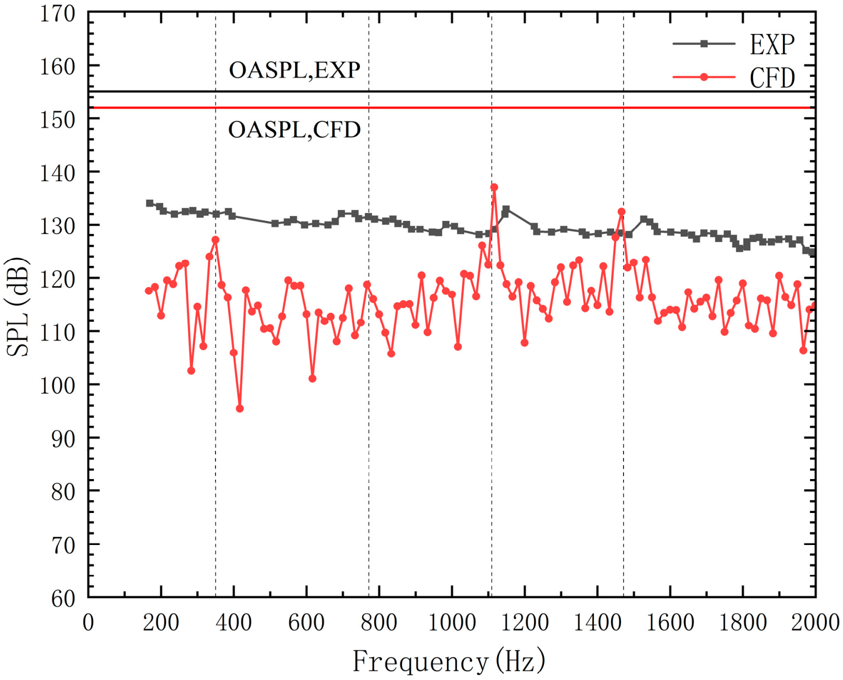

Figure 4. Comparison of simulated and experimental cavity sound pressure levels at the K18 point.

Table 1. Noise data comparison at monitoring point K18.

	Modal	**1_{st}**	**2_{nd}**	**3_{rd}**	**4_{th}**
Experiment	Frequency (Hz)	287	695	1152	1527
	Sound Pressure Level (dB)	132.5	132.1	132.8	131
CFD	Frequency (Hz)	349.9	766.5	1116	1466.4
	Sound Pressure Level (dB)	127.1	118.8	137.1	132.4

As shown in Figure 5, the horizontal axis represents frequency, while the vertical axis represents power spectral density (PSD). PSD reflects the power distribution of noise components at different frequencies. From the figure, it is evident that the contributions of first-, second-, third-, and fourth-order modes to OASPL can be clearly observed. The impact of the third- and fourth-order modes on OASPL is significantly greater than that of the first- and second-order modes. Therefore, we believe that our simulation method is reliable overall.

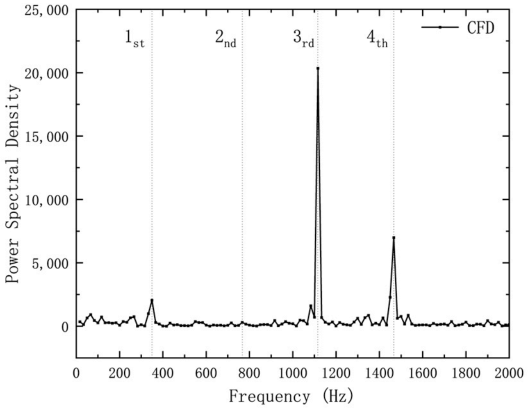

Figure 5. Power spectral density at point K18.

3.2. Validation of the Plasma Actuator Model

To validate the plasma phenomenological model, we turn to a comprehensive case study and subject the computational results to rigorous comparison with the experimental data in reference [32] so we can ascertain the method's ability to replicate the observed phenomena and trends. Through this validation process, we gain confidence in the predictive capabilities of the plasma actuator model, paving the way for its application in unraveling the complex cavity flows. In the subsequent section, we will delve into the outcomes of our plasma-related simulations, shedding light on the impact of plasma actuation on cavity flow characteristics.

Based on reference [32], the upper electrode is positioned on a two-dimensional flat plate, as depicted in Figure 6. The total length of the plate is 20.5 mm, and the incoming flow velocity is U_∞ = 5 m/s, aligned parallel to the plate surface along the positive X-axis direction. Sections ST1, ST2, ST3, and ST4 are located at distances of 4.75 mm, 12 mm, 13.9 mm, and 17.3 mm from the leading-edge wall, respectively, as illustrated in Figure 6.

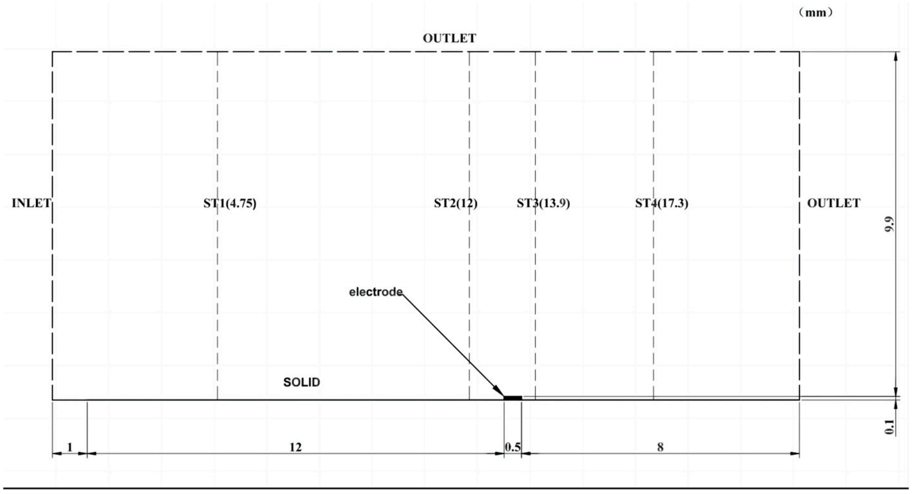

Figure 6. Computational domain of the two-dimensional model.

The validation of the computational results is shown in Figure 7, where the horizontal axis represents the magnitude of the X-direction velocity, and the vertical axis represents the height of the vertical wall. From Figure 7, it can be observed that for cross-sections ST1, ST2, and ST3, the maximum error occurs at a distance of 0.63mm from the wall. The maximum error for each of these sections is less than 9%, and the errors at other points are all below 6%. For cross-section ST4, the maximum error occurs at a distance of 0.857mm from the wall, with an error of 8.17%. The errors at other points are also below 6%. These results indicate a good agreement between our computational findings and the reference [32], demonstrating an accurate simulation of the plasma's excitation effects on the flow field.

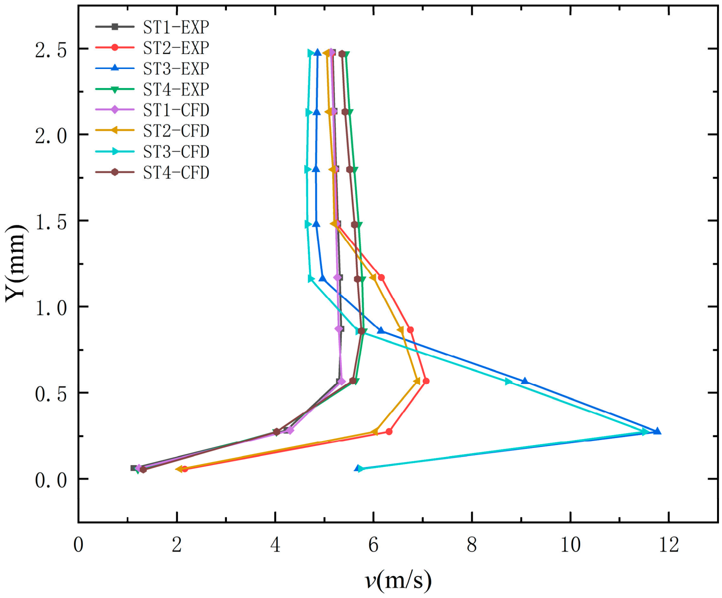

Figure 7. Comparison of the X-component velocities at different sections between the literature data and the validation computation.

In summary, the plasma phenomenological model emerges as a powerful tool in our arsenal, enabling us to delve deep into the effects of the plasma actuator on the cavity flows. The integration of experimental findings into the computational framework marks a pivotal advancement, allowing us to unravel the intricate flow control mechanisms with a high degree of accuracy and fidelity.

4. The High-Speed Cavity Model and Independence Analysis

4.1. The Studied High-Speed Cavity Model

The two-dimensional cavity designed in this study (as shown in Figure 8) has a length of 4.2 m and a depth of 0.6 m, with an aspect ratio (L/D) of seven, falling within the category of typical long-depth ratio configurations for open cavity flows. The chosen operating condition corresponds to Ma = 4 and atmospheric parameters at an altitude of 25 km, aiming to simulate the aerodynamic noise characteristics of a high-Mach-number cavity. Along the upstream direction, a total of 10 pressure monitoring points, labeled as K20-K29, are uniformly distributed along the bottom surface of the cavity within the region of *x*/*L* = 0.05 to 0.95. These monitoring points are strategically placed to measure the variations in internal cavity noise.

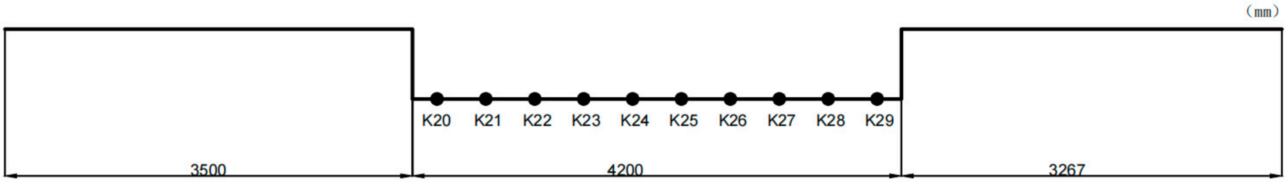

Figure 8. Two-dimensional cavity model and location of monitoring points.

4.2. Grid Independence Analysis

Grid independence analysis is crucial for ensuring the accuracy and reliability of numerical simulations. In our study of cavity flows and plasma-induced flow control, this analysis is essential to validate the robustness of our simulation framework. The main purpose of grid independence analysis is to confirm that our results are not heavily influenced by the choice of grid resolution. By systematically varying the grid and observing the convergence of flow features, we can ensure that our findings are consistent and accurate. This analysis is especially important for capturing the intricate interactions in cavity flows, especially vortices. Moreover, grid independence analysis helps optimize computational resources. Striking a balance between grid resolution and efficiency is key to obtaining meaningful results without excessive computational costs. By identifying the minimum grid refinement needed for convergence, we can ensure efficient simulations.

The computational conditions include an incoming flow velocity of Ma = 4, a static pressure of $P\infty$ = 2509.98 Pa, and a static temperature of T = 93.08 K. The chosen time step for simulations is 5×10^{-5} s. To investigate grid independence, the cavity grid model is divided into four sets with varying grid densities labeled as Models A, B, C, D, and E, corresponding to grid quantities of 69,000, 126,000, 163,000, 210,000, and 300,000, respectively.

Figure 9 illustrates a comparison of the total sound pressure level at ten monitoring points distributed along the cavity bottom surface for the four mesh models. Among these, Models C, D, and E exhibit relatively close results, while Models A and B fail to accurately predict the increase in the total sound pressure level at x/L = 0.25 and the decrease at x/L = 0.85. As the grid quantity reaches approximately 163,000, the trend in internal cavity noise stabilizes, and the total sound pressure level error becomes sufficiently small. Considering computational cost and resources, Model C is selected for subsequent investigations.

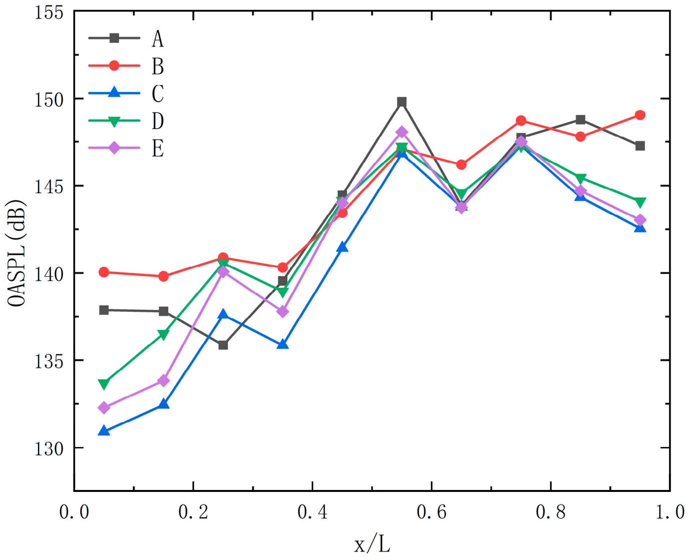

Figure 9. Sound pressure level data at the bottom of the cavity for different meshes.

4.3. Time Step Independence Analysis

In the realm of numerical simulations, investigating the independence of results with respect to the chosen time step is paramount. Time step independence analysis, akin to grid independence analysis, plays a crucial role in affirming the reliability and accuracy of our computational findings. The essence of time step independence analysis lies in comprehending the impact of temporal discretization on simulated flow behavior. A smaller time step might provide greater temporal resolution, capturing intricate flow features with precision. However, excessively small time steps can escalate computational costs substantially. Conversely, a larger time step may offer computational efficiency but could potentially lead to the loss of critical flow details.

By systematically varying the time step size and observing the convergence of relevant flow parameters, we can ascertain the appropriate temporal discretization for our simulations. This ensures that our numerical results are not unduly influenced by the choice of time step, strengthening the credibility of our investigation into cavity flows and plasma-induced flow control. Time step independence analysis also facilitates a balance between accuracy and computational efficiency. Achieving convergence with a reasonable time step optimizes the utilization of computational resources while providing accurate insights into the temporal evolution of flow phenomena.

In the upcoming section, we will elaborate on our approach to time step independence analysis for the selected Model C considering five distinct time step values.

Figure 10 displays the computational results obtained using the five different time steps: 2×10^{-4} s, 1×10^{-4} s, 8×10^{-5} s, 5×10^{-5} s, and 2.5×10^{-5} s. As depicted in the figure, when the time step exceeds 5×10^{-5} s, the total sound pressure levels at each monitoring point tend to be higher. Conversely, when the time step is less than 5×10^{-5} s, the variations in sound pressure levels at the monitoring points stabilize in terms of both trend and magnitude. Therefore, the time step of 5×10^{-5} s, which offers higher computational efficiency, is employed for the numerical simulations.

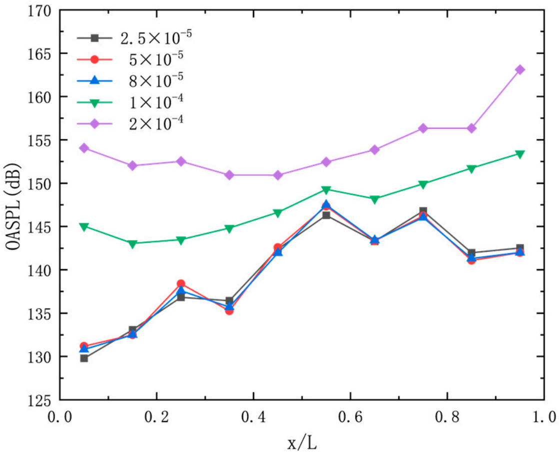

Figure 10. Sound pressure level data at the bottom of the cavity for different time steps.

5. Noise Prediction and Plasma-Based Control of Cavity Flows

5.1. Calculation Setups

In this section, the DBD plasma actuator is employed with parameters identical to those specified in reference [32]. The actuation region has dimensions a = 1.5 mm and b = 3 mm, operating at a voltage frequency of 3000 Hz, with a charge density of 1×10^{11} cm^3, and the elementary electron charge e = 1.602×10^{-19}. The discharge duration is 67 µs, and the breakdown electric field strength at the electric field boundary is set at 30 kV/cm. The distance between the electrodes is 0.25 mm, and the initial excitation voltage is 4 kV. The plasma actuation effect is incorporated into the Navier–Stokes equations as a volumetric force source term.

The incoming flow conditions remain consistent with those described in Section 2, utilizing the same numerical simulation methodology. The mesh quantity is based on Model C (as shown in Figure 11) as a baseline of 163,000 cells. Mesh refinement is applied within the plasma actuation region (as shown in Figure 12), resulting in a final mesh quantity of approximately 200,000 cells. The time step is set to 5×10^{-5} s, totaling 20,000 steps. The initial 6000 steps are discarded to eliminate initial oscillations.

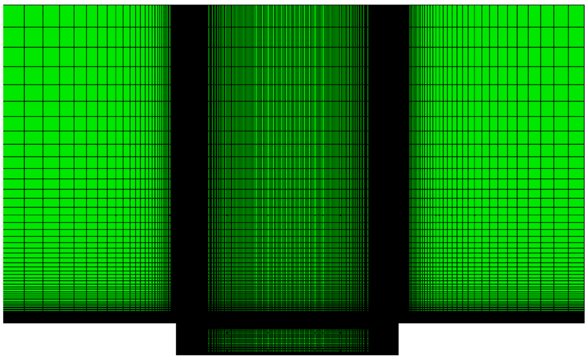

Figure 11. Cavity mesh configuration.

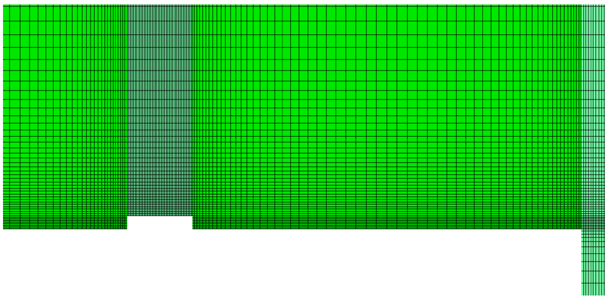

Figure 12. Plasma actuator mesh configuration.

In accordance with the diagram presented in Figure 13, the boundary conditions for the numerical simulation are configured as follows: boundary a, b, and c represent the pressure far-field conditions, enabling the flow to exit the computational domain smoothly without introducing any disturbances. Boundary d corresponds to the wall condition, characterized by a no-slip constraint, which ensures that the flow does not penetrate or slip through the solid boundary. The height of the computational domain extends 10 times the cavity depth based on the dimensions of the design model.

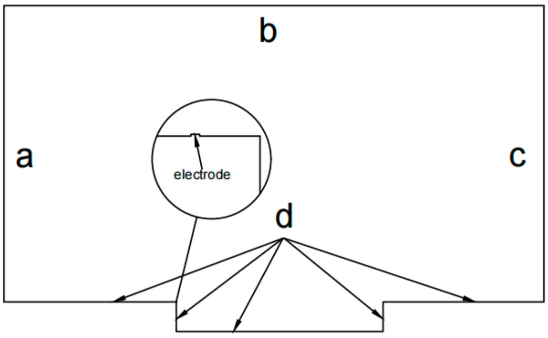

Figure 13. Boundary conditions of the plasma-excited cavity model.

5.2. *Aerodynamic and Acoustic Characteristics of the Uncontrolled Cavity*

Figure 14 illustrates the OASPL distribution at ten positions along the cavity bottom, ranging from K20 to K29. Notably, there are three distinct peaks in the OASPL, and the highest OASPL occurs at point K25, corresponding to x/L = 0.55.

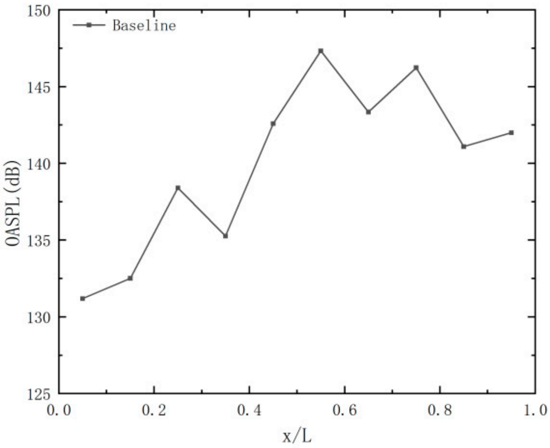

Figure 14. OASPL at various monitoring points along the bottom of the uncontrolled cavity.

In Figure 15, we can observe that the flow pattern in the examined cavity exhibits typical characteristics of open cavity flow. The airflow separates at the cavity's leading edge, part of it entering the cavity while the rest forms a shear layer above. This shear layer extends over the central part of the cavity and then reattaches at the trailing edge. Importantly, there are multiple peaks in the global sound pressure level, both at the front (*x/L* = 0.25) and rear (x/L = 0.55, *x/L* = 0.75) sections of the cavity.

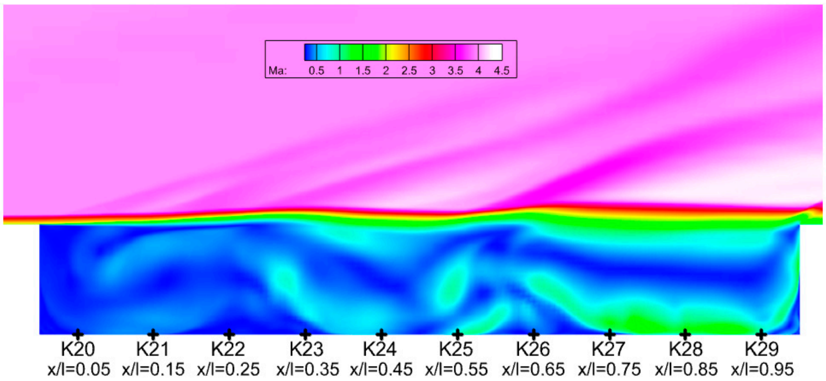

Figure 15. Mach number contour map of the uncontrolled cavity flow.

Figure 16 shows vorticity maps at different phases within a single cycle using the Q-criterion, as indicated in Figure 16a, which illustrates the vorticity direction. In Figure 16a, a sequence of alternating clockwise and counterclockwise vortices can be observed in the incoming flow direction within the cavity. These vortices alternate with smaller vortices of opposite directions, and the entire flow process involves both the breakdown of larger vortices and the merging of smaller ones.

At a specific moment, denoted as T (representing a single flow cycle's duration), several vortex interactions occur. Firstly, a counterclockwise small vortex E detaches from a clockwise large vortex B, moving along the negative X direction of the cavity bottom. Eventually, it merges with the counterclockwise large vortex A at its upper section. Simultaneously, vortex C and vortex F combine as well. Vortex F, which is a counterclockwise small vortex resulting from the detachment of a clockwise large vortex D near the cavity's rear wall along the negative X direction of the bottom, moves to the upper part of the counterclockwise large vortex C. This results in the complete fusion of vortex C and F. Following the collision of the shear layer with the rear cavity wall, a large vortex D forms. As vortex F periodically merges with vortex C, shed from the large vortex D, the dissipative and fusion processes allow vortex C to remain stable within the cavity flow. However, its position in the X direction undergoes periodic variations.

A noticeable observation is the relative stability of vortices at the front of the cavity, where vortex fusion is minimal within a single cycle. In contrast, the middle and rear portions of the cavity are more susceptible to vortex breakdown and fusion phenomena. Interestingly, the locations of vortex breakdown and fusion roughly align with regions where extreme values of cavity OASPL noise occur. It can be inferred that vortex breakdown and fusion play a significant role in the generation of aerodynamic noise.

5.3. Influence of Excitation Voltage

In order to investigate the impact of excitation voltage on noise control effectiveness, numerical simulations are conducted with varying excitation voltages at the same excitation frequency. The specific excitation voltage settings are presented in Table 2.

Table 2. Excitation voltage configuration.

Case	**1**	**2**	**3**	**4**	**5**	**6**	**7**
Excitation Frequency (kHz)				3			
Excitation Voltage (kV)	4	6	8	10	12	14	16

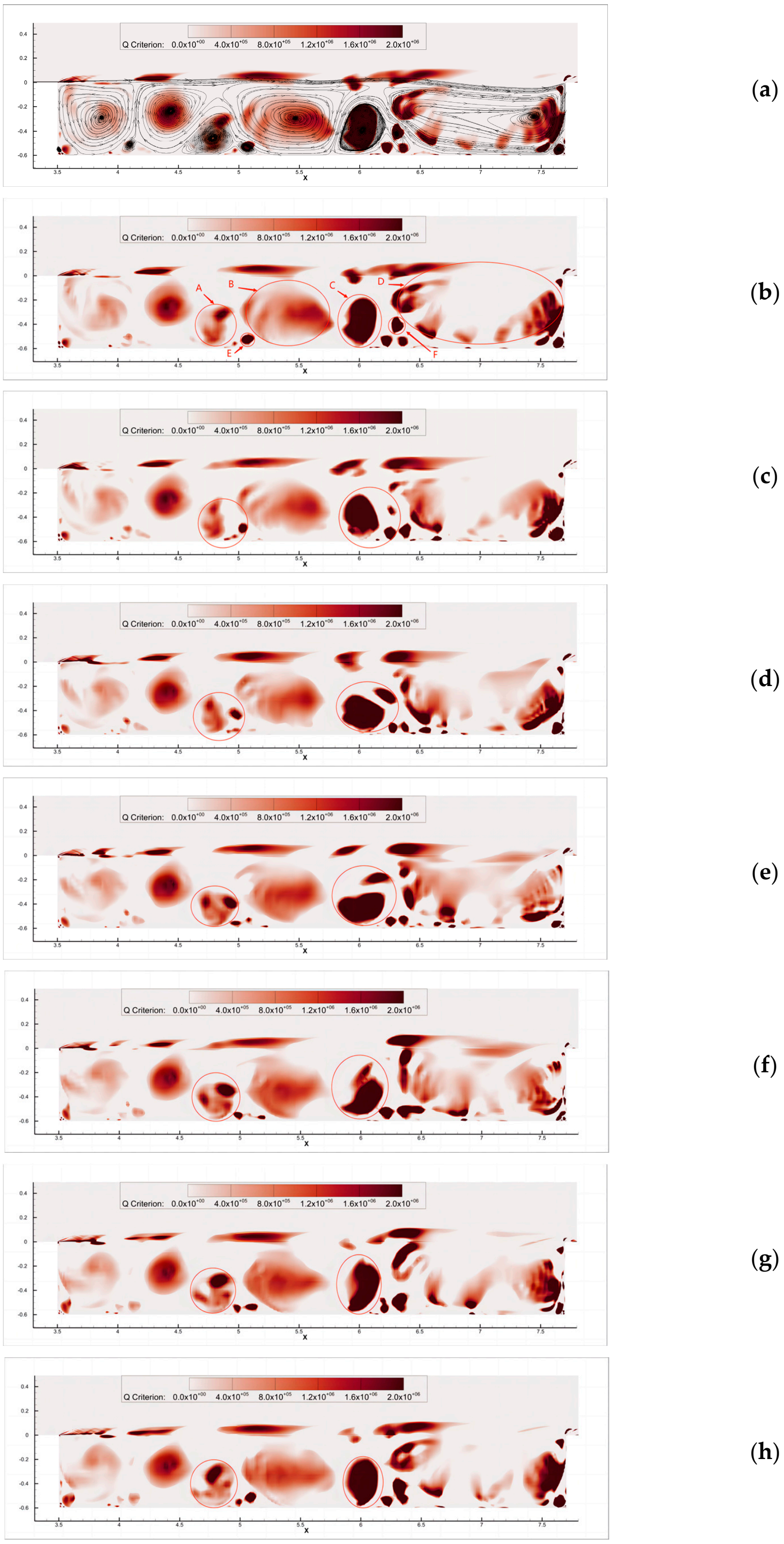

(**a**)

(**b**)

(**c**)

(**d**)

(**e**)

(**f**)

(**g**)

(**h**)

Figure 16. Vorticity contour plot of the uncontrolled cavity flow: (**a**) $t = \frac{1}{7}$T, (vortex rotation direction); (**b**) $t = \frac{1}{7}$T; (**c**) $t = \frac{2}{7}$T; (**d**) $t = \frac{3}{7}$T; (**e**) $t = \frac{4}{7}$T; (**f**) $t = \frac{5}{7}$T; (**g**) $t = \frac{6}{7}$T; (**h**) t = T.

Figure 17 shows the changes in the total sound pressure level at various monitoring points along the bottom of the cavity under different excitation voltages at a constant excitation frequency of 3 kHz. With the exception of point K28 (x/L = 0.85), the optimal excitation voltage is found to be 12 kV. At point K20 (x/L = 0.05), the maximum reduction can be 3.073 dB. Notably, different excitation voltages do not effectively reduce the global sound pressure level at point K28 (x/L = 0.85).

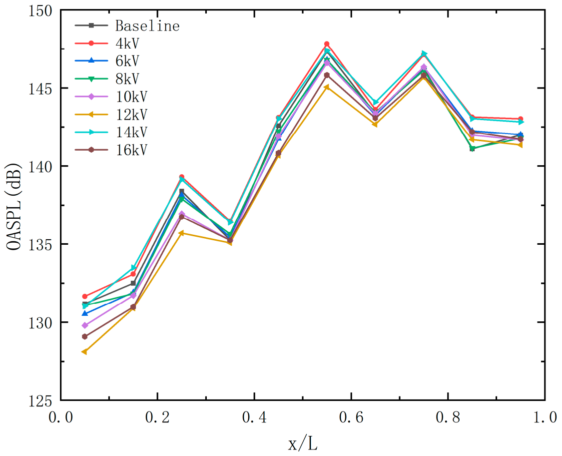

Figure 17. OASPL values at different monitoring points along the bottom surface of the cavity under different excitation voltages.

In Figure 18, we observe the variation in OASPL at point K25 under different excitation voltages while maintaining a consistent excitation frequency of 3 kHz. When the excitation voltage is set at 4 kV, a noticeable increase in high-frequency noise levels is observed, resulting in an overall rise in OASPL. As the excitation voltage gradually increases from 6 kV to 12 kV, there is a slight reduction in SPL amplitude in both the low-frequency range (≤100 Hz) and the high-frequency range (≥1000 Hz), despite the SPL value of the dominant mode at 315 Hz remaining relatively stable. These combined effects contribute to the decrease in OASPL at point K25 from 147.329 dB under uncontrolled conditions to 145.057 dB under 12 kV excitation voltage.

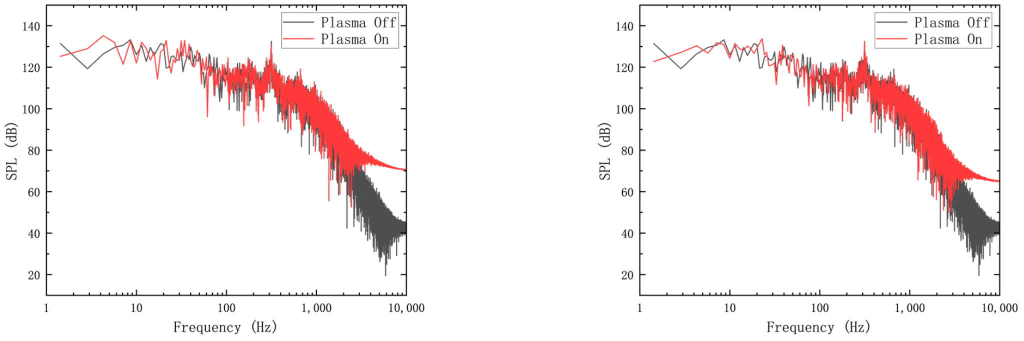

(**a**) V = 4 kV (**b**) V = 6 kV

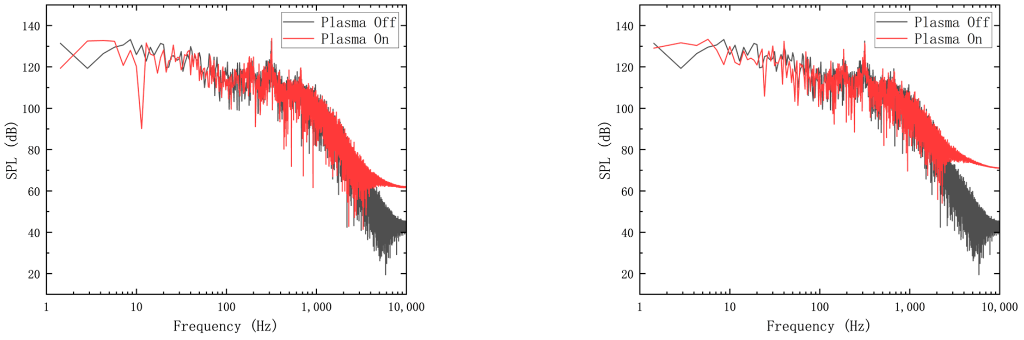

(**c**) V = 8 kV (**d**) V = 10 kV

Figure 18. *Cont.*

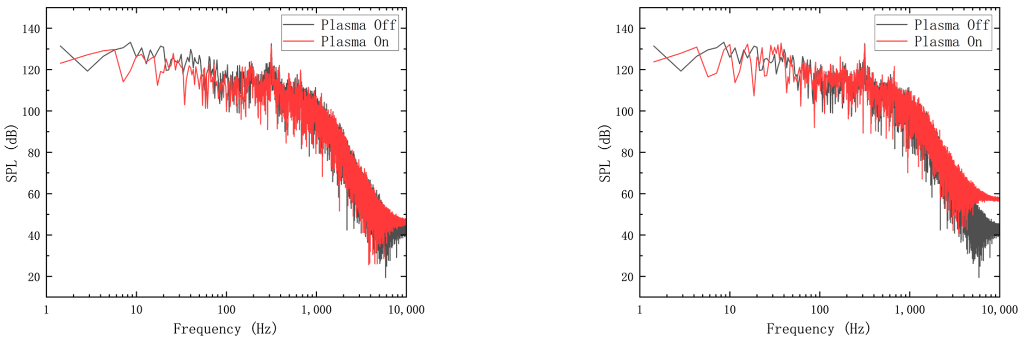

(**e**) V = 12 kV (**f**) 14 kV

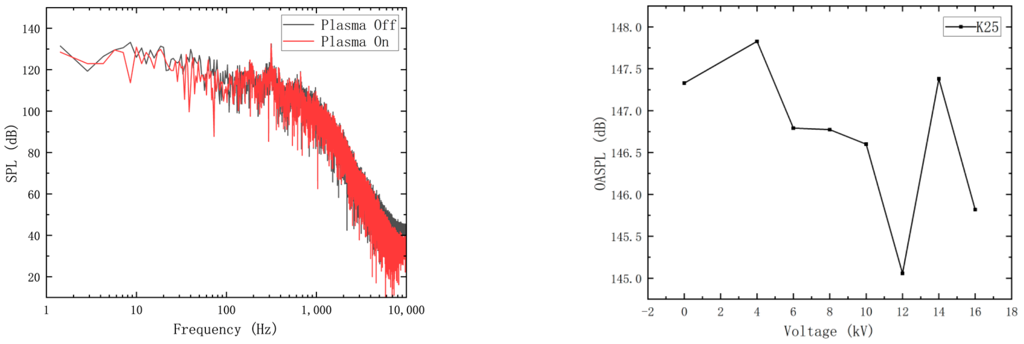

(**g**) V = 16 kV (**h**)

Figure 18. Noise characteristics at point K25 under different excitation voltages: (**a**) f = 3 kHz, V = 4 kV; (**b**) f = 3 kHz, V = 6 kV; (**c**) f = 3 kHz, V = 8 kV; (**d**) f = 3 kHz, V = 10 kV; (**e**) f = 3 kHz, V = 12kV; (**f**) f = 3 kHz, V = 14 kV; (**g**) f = 3 kHz, V = 16 kV; (**h**) OASPL of different voltages of excitation.

However, at 14 kV excitation voltage, there is a notable increase in SPL amplitude in the high-frequency range, resulting in an increase in OASPL to 147.38 dB. When the excitation voltage is further increased to 16 kV, the frequency distribution characteristics resemble those observed at a 12 kV excitation voltage, leading to a decrease in OASPL to 145.819 dB.

To investigate whether plasma excitation impacts the internal noise of the cavity by altering the boundary layer thickness, we conducted measurements of the boundary layer thickness at the leading edge of the cavity lip. These measurements were taken at excitation voltages of 4 kV, 6 kV, 8 kV, 10 kV, 12 kV, 14 kV, and 16 kV, all at a frequency of 3 kHz. The results consistently indicated that the boundary layer thickness remained approximately 50mm under different excitation voltages. This suggests that plasma voltage excitation does not significantly affect noise levels at various points within the cavity by modifying the boundary layer thickness.

In Figure 19, the variation of the relative limit position of the dominant vortex throughout the entire flow duration (t = 0.3–1 s) is depicted for different excitation voltages, as indicated by the red circles. The figures (a,c,e,g,i,k) in Figure 19 show the left limit position of the dominant vortex under different excitation voltages. Meanwhile, the figures (b,d,f,h,j,l) in Figure 19 show the left limit position of the dominant vortex under different excitation voltages. The occurrence time of the dominant vortex's limit position can be influenced by different excitation voltages and variations in timing. It can be observed that the flow pattern within the cavity remains consistent and the vortex system structure undergoes negligible changes under different voltage levels. The position of the vortices within the cavity remains relatively stable over one cycle. However, due to the continuous interaction with the shear layer impinging on the rear wall, the positions of the vortex experience some displacement over multiple flow cycles. This displacement leads to an alteration in the extent of vortex shedding and collapse, resulting in an expansion or contraction of the radiating region, as indicated by the shifting of the red circles. It is evident that the stability of the dominant vortex position, as demonstrated by the red circles, influences OASPL of the K25 point.

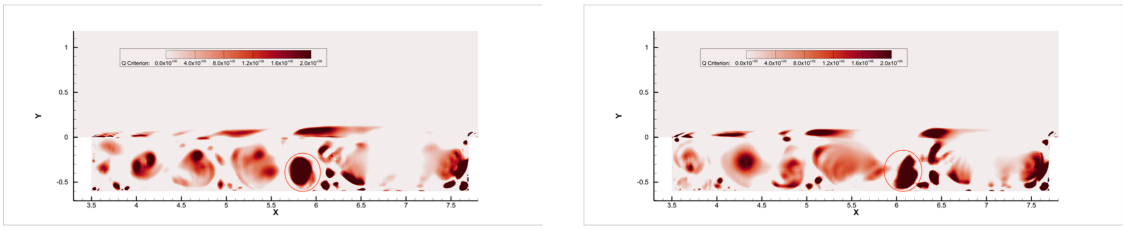

(**a**) V = 0 kV (**b**) V = 0 kV

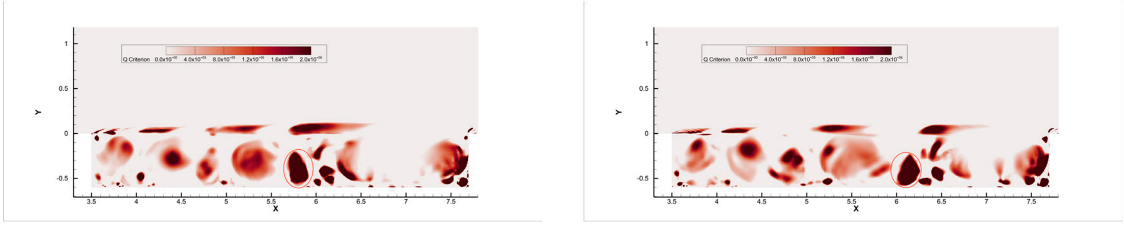

(**c**) *V* = 4 kV (**d**) *V* = 4 kV

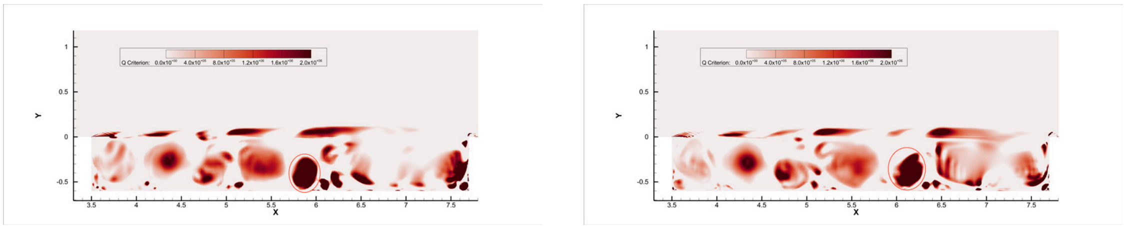

(**e**) V = 6 kV (**f**) V = 6 kV

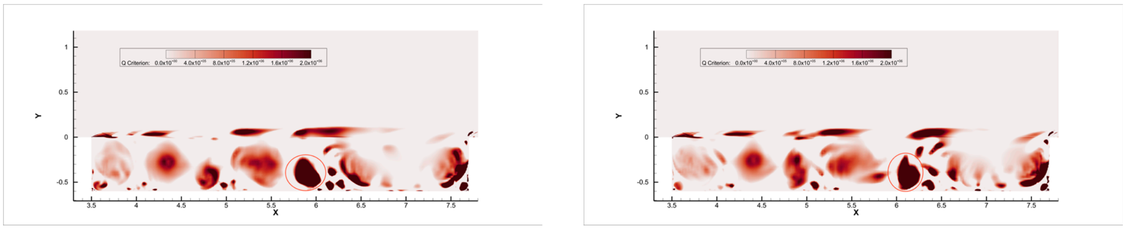

(**g**) V = 12 kV (**h**) V = 12 kV

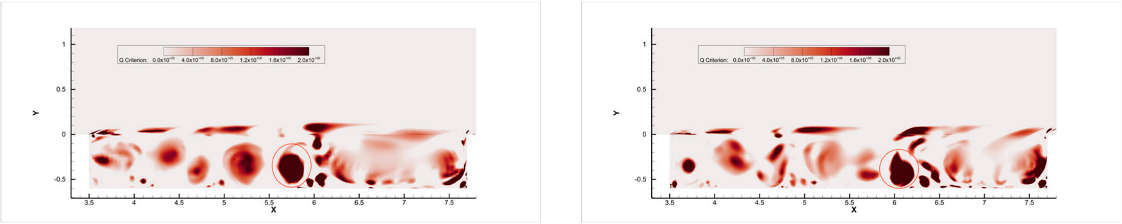

(**i**) V = 14 kV (**j**) V = 14 kV

Figure 19. *Cont.*

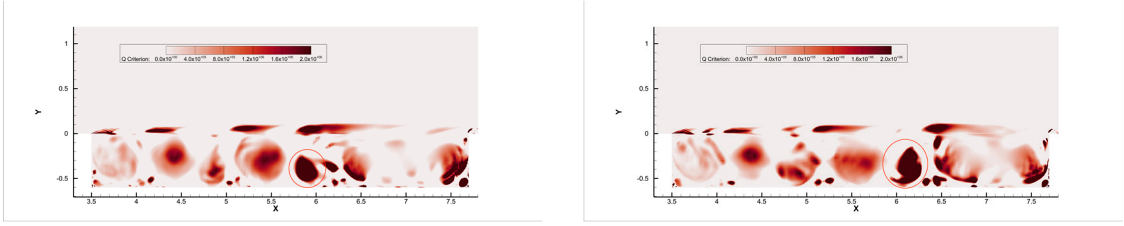

(**k**) V = 16 kV (**l**) V = 16 kV

Figure 19. Contour plot of cavity vorticity under different excitation voltages: (**a**) $V = 0$ kV, left limit position; (**b**) $V = 0$ kV, left limit position; (**c**) $V = 4$ kV, right limit position; (**d**) $V = 4$ kV, right limit position; (**e**) $V = 6$ kV, left limit position; (**f**) $V = 6$ kV, right limit position; (**g**) $V = 12$ kV, left limit position; (**h**) $V = 12$ kV, right limit position; (**i**) $V = 14$ kV, left limit position; (**j**) $V = 14$ kV, right limit position; (**k**) $V = 16$ kV, left limit position; (**l**) $V = 16$ kV, right limit position.

Table 3 presents the corresponding data between the OASPL values at the K25 point and the X-direction displacement range of the characteristic vortex for various excitation voltages. It can be observed that there exists a positive correlation between the OASPL values and the X-direction displacement range of the vortex under different excitation voltages. As the relative displacement becomes smaller, the vortex structure exhibits higher stability, leading to reduced high-frequency noise caused by vortex shedding and merging, ultimately resulting in a lower total sound pressure level.

Table 3. Dominant vortex X-direction displacement range and corresponding OASPL data under different excitation voltages.

Excitation Voltage (kV)	**0**	**4**	**6**	**12**	**14**	**16**
OASPL (dB)	147.329	147.827	146.791	145.057	147.38	145.819
X-direction Displacement Range (mm)	304.8	347.6	276.5	239.6	338.2	267.8

5.4. Effect of Excitation Frequency

To investigate the influence of excitation frequency on noise control effectiveness, numerical simulations were conducted with different excitation frequencies under the same excitation voltage, as shown in Table 4.

Table 4. Excitation frequency conditions.

Case	**8**	**9**	**10**	**11**	**12**
Excitation Voltage (kV)			4		
Excitation Frequency(kHz)	3	6	9	12	15

Figure 20 illustrates the impact of different excitation frequencies on the OASPL at points K20 to K29. It can be observed that the aerodynamic noise level at the K25 point does not exhibit a significant decrease under different plasma excitation frequencies. In some cases, such as f = 3 kHz and f = 12 kHz, the OASPL even increased by approximately 0.5 dB. Notably, as depicted in Figure 21, with increasing plasma excitation frequency, its effect on the mid- to low-frequency range (below 1000 Hz) is relatively small. The dominant mode around 315 Hz is minimally affected, and in the high-frequency range, plasma excitation may even amplify the SPL values, leading to an increase in OASPL. When the excitation frequency is 15 kHz, the SPL amplitude decreases in the mid-frequency range (100~200 Hz) and slightly increases in the high-frequency range, causing the K25 point's OASPL to decrease from 147.329 dB to 146.407 dB. In comparison to the influence of excitation voltage, the effect of excitation frequency is less significant. Similarly, variations in excitation frequency do not notably change the frequency and SPL amplitude of the dominant mode but primarily affect the SPL amplitude at high frequencies.

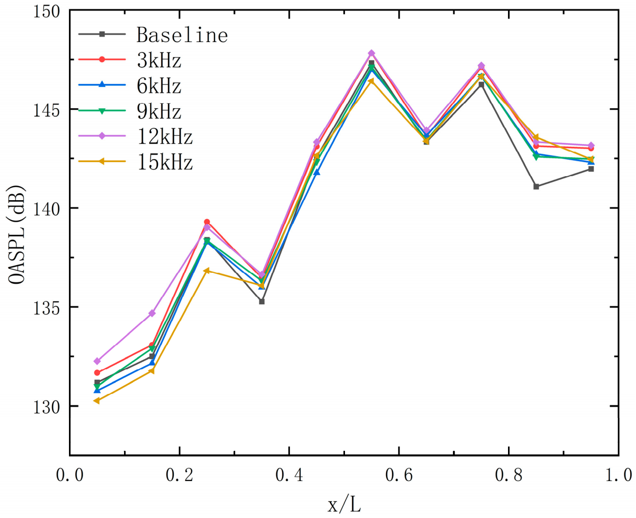

Figure 20. OASPL distribution at different bottom surface monitoring points for various excitation frequencies.

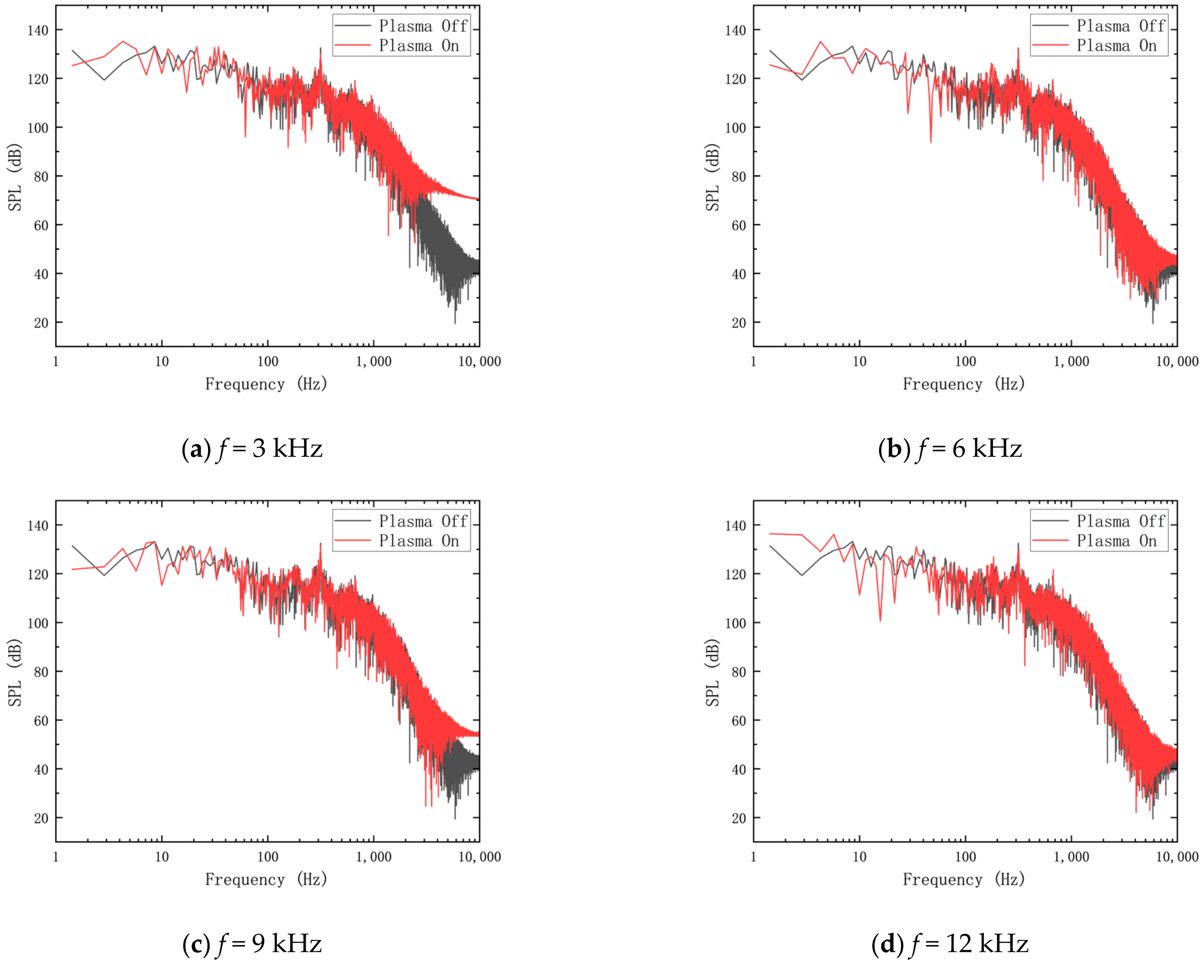

(**a**) $f = 3$ kHz (**b**) $f = 6$ kHz

(**c**) $f = 9$ kHz (**d**) $f = 12$ kHz

Figure 21. *Cont.*

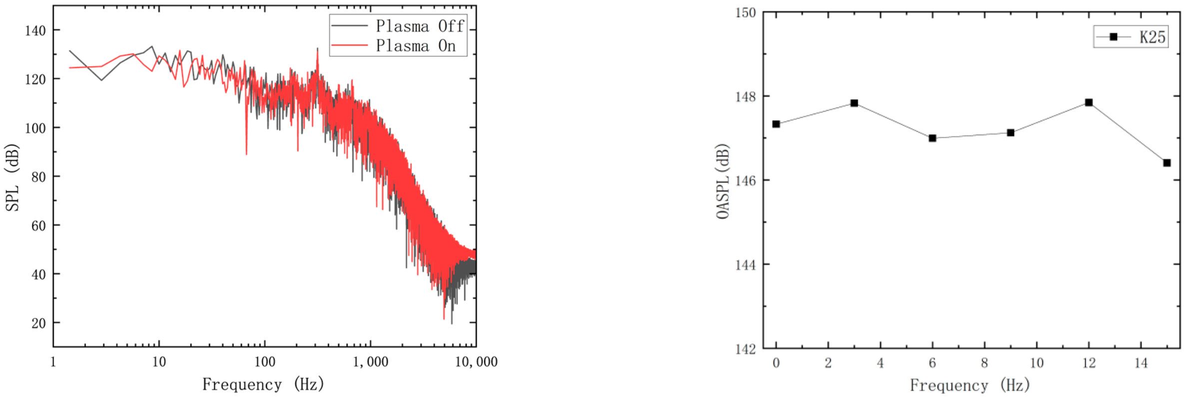

(**e**) *f* = 15 kHz (**f**)

Figure 21. Noise variation characteristics at monitoring point K25 for different excitation frequencies: (**a**) f = 3 kHz, V = 4 kV; (**b**) f = 6 kHz, V = 4 kV; (**c**) f = 9 kHz, V = 4 kV; (**d**) f = 12 kHz, V = 4 kV; (**e**) f = 15 kHz, V = 4 kV; (**f**) OASPL of different frequency of excitation.

We measured the boundary layer thickness at the lip of the cavity leading edge corresponding to excitation voltages of 3 kHz, 6 kHz, 9 kHz, 12 kHz, and 15 kHz, all at an excitation voltage of 4 kV. The results indicate that the boundary layer thickness remains consistent at approximately 50 mm across different excitation frequencies. It can be observed that the effect of the plasma excitation frequency on the boundary layer thickness is similar to the situation with excitation voltage; it does not produce a significant influence. This suggests that plasma excitation does not primarily impact the cavity noise level by altering the boundary layer thickness.

Building upon the findings from the previous section, we proceed to observe the behavior characteristics of the dominant vortex near point K25. As illustrated in Figure 22, the left and right extreme positions of the dominant vortex are presented throughout the entire flow duration (t = 0.3—1 s) for different excitation frequencies. Figures (a,c,e) in Figure 22 illustrate the left limit position of the dominant vortex under different excitation frequencies. Similarly, Figures (b,d,f) in Figure 22 depict the left limit position of the dominant vortex under different excitation frequencies. The occurrence time of the dominant vortex's limit position can be influenced by different excitation frequencies and variations in timing. It is evident that the flow pattern within the cavity remains consistent, and the vortex system structure undergoes minimal changes across different voltage levels. The positions of the vortices within the cavity exhibit relative stability over a single cycle, aligning with the observed trend in plasma excitation voltage.

Table 5 provides a comparison of the OASPL values at point K25 for different excitation frequencies and the corresponding X-direction displacement range of the dominant vortex. It is evident that the X displacement of the dominant vortex is positively correlated with their OASPL magnitude, similar to the observed trend with plasma excitation voltage. A smaller relative displacement indicates a more stable vortex structure, resulting in reduced high-frequency noise generated by vortex shedding and merging.

Table 5. X-direction displacement range of dominant vortex and corresponding OASPL data at different excitation frequencies.

Excitation Frequency (kHz)	0	3	12	15
OASPL (dB)	147.329	147.827	147.843	146.407
X-direction Displacement Range (mm)	304.8	347.6	374.9	262.5

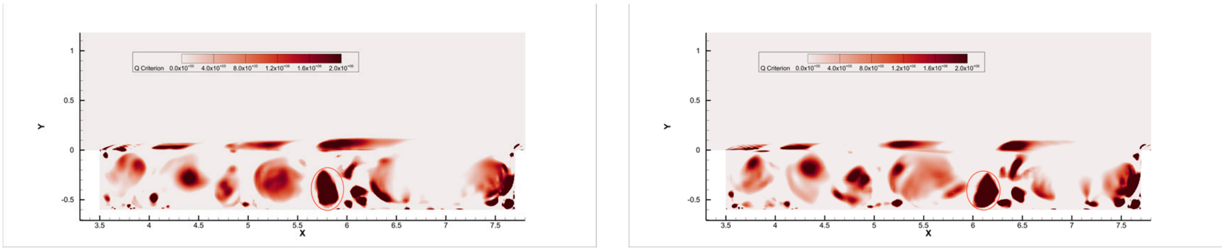

(**a**) $f = 3$ kHz (**b**) $f = 3$ kHz

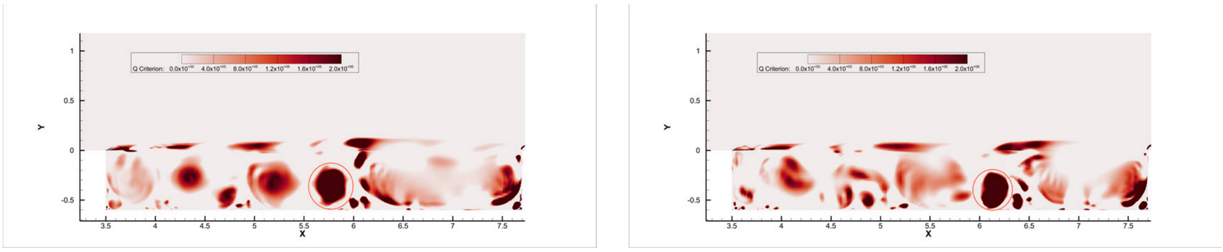

(**c**) $f = 12$ kHz (**d**) $f = 12$ kHz

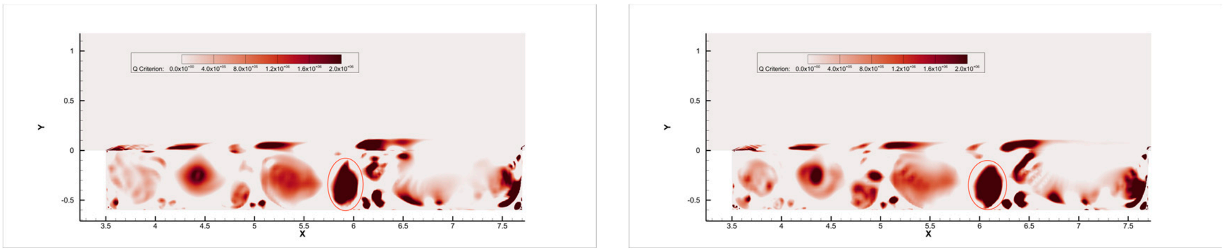

(**e**) $f = 15$ kHz (**f**) $f = 15$ kHz

Figure 22. Contour plot of cavity vorticity under different excitation frequencies: (**a**) $f = 3$ kHz, left limit position; (**b**) $f = 3$ kHz, right limit position; (**c**) $f = 12$ kHz, left limit position; (**d**) $f = 12$ kHz, right limit position; (**e**) $f = 15$ kHz, left limit position; (**f**) $f = 15$ kHz, right limit position.

6. Conclusions

In this study, the primary objective is to investigate the acoustic characteristics and noise reduction strategies of a rectangular cavity under high-Mach-number conditions. Through comprehensive simulations conducted at Mach 4, employing a cavity with dimensions of 4.2×0.6 m^2, the influence of plasma-based control on noise reduction was meticulously studied. The following key conclusions can be drawn from the conducted research:

1. This paper studies the suppression of aerodynamic noise in high-speed cavities using a combined DDES and DBD method for the first time. Comparing with experimental data, the calculation error of the OASPL in high-speed cavities is within 2%, and the calculation error of the X-direction velocity of the plasma actuator model is within 9%.
2. The cavity with L/D = 7 exhibits distinct open flow characteristics at Ma=4 and an altitude of 25 km. Multiple OASPL peaks are observed in the front, middle, and rear regions of the cavity. The maximum OASPL reaches 147.329 dB, occurring at $x/L = 0.55$. The locations of vortex breakdown and fusion correspond to the regions and roughly align with regions where extreme values of cavity noise occur.
3. Relative to the excitation frequency, the excitation voltage of the plasma actuator has a more pronounced effect on noise suppression. Appropriate excitation voltage can reduce the OASPL by up to 2.27 dB by suppressing low-frequency noise. The

excitation voltage can reduce the sound pressure level amplitude of the dominant mode, thereby decreasing the OASPL of the high-speed cavity.

4. The effect of the excitation frequency of the plasma actuator on noise suppression is weaker, yet an optimal frequency exists. Variations in the excitation frequency have a less noticeable impact on the frequency and sound pressure level amplitude of the dominant mode, primarily affecting high-frequency sound pressure levels, with a maximum reduction of 0.336 dB in the OASPL.
5. Plasma actuators can alter the lateral movement range of the dominant vortex within the high-speed cavity. As the lateral displacement of the dominant vortex decreases, the OASPL of the cavity also decreases.

Author Contributions: Conceptualization, H.C., Z.Z. and Z.L.; methodology, H.C. and Z.Z.; software, H.C. and Z.Z.; validation, H.C., Z.Z. and H.L.; formal analysis, H.C. and Z.Z.; investigation, H.C., Z.Z. and Z.L.; data curation, H.C. and Z.Z.; writing—original draft preparation, H.C., Z.Z. and Z.L.; writing—review and editing, H.C., Z.Z. and H.L.; All authors have read and agreed to the published version of the manuscript.

Funding: This work was supported by Aeronautical Science Foundation of China (Grant No. 2020Z006052001), Rotor Aerodynamics Key Laboratory Fund Project (RAL20190101), and the Fundamental Research Funds for the Central Universities (Grant No.1011-YAH21001).

Data Availability Statement: Not applicable.

Conflicts of Interest: The authors declare that there is no conflict of interest.

References

1. Rowley, C.W.; Williams, D.R. Dynamics and Control of High-Reynolds-Number Flow over Open Cavities. *Annu. Rev. Fluid Mech.* **2006**, *38*, 251–276. [CrossRef]
2. Heller, H.; Delfs, J. Cavity Pressure Oscillations: Cavity Pressure Oscillations: The Generating Mechanism Visualized. *Lett. Ed. J. Sound Vib.* **1996**, *196*, 248–252. [CrossRef]
3. Lee, B.H.K. Effect of Captive Stores on Internal Weapons Bay Floor Pressure Distributions. *J. Aircr.* **2010**, *47*, 732–736. [CrossRef]
4. Lawson, S.J.; Barakos, G.N. Review of Numerical Simulations for High-Speed, Turbulent Cavity Flows. *Prog. Aerosp. Sci.* **2011**, *47*, 186–216. [CrossRef]
5. Knotts, B.D.; Selamet, A. Suppression of Flow–Acoustic Coupling in Sidebranch Ducts by Interface Modification. *J. Sound Vib.* **2003**, *265*, 1025–1045. [CrossRef]
6. Zhuang, N. Experimental Investigation of Supersonic Cavity Flows and their Control. Ph.D. Thesis, The Florida State University, Tallahassee, FL, USA, 2007. Available online: https://www.proquest.com/dissertations-theses/experimental-investigation-supersonic-cavity/docview/304872228/se-2 (accessed on 24 October 2023).
7. Heller, H.; Bliss, D.B. *Aerodynamically Induced Pressure Oscillations in Cavities: Physical Mechanisms and Suppression Concepts*; Wright-Patterson Air Force Base: Dayton, OH, USA, 1975.
8. Schmit, R.; Semmelmayer, F.; Grove, J.; Haverkamp, M. Fourier Analysis of High Speed Shadowgraph Images Around a Mach 1.5 Cavity Flow Field. In Proceedings of the 29th AIAA Applied Aerodynamics Conference, Honolulu, HI, USA, 27–30 June 2011; American Institute of Aeronautics and Astronautics: Washington, DC, USA, 1996. [CrossRef]
9. Handa, T.; Miyachi, H.; Kakuno, H.; Ozaki, T. Generation and Propagation of Pressure Waves in Supersonic Deep-Cavity Flows. *Exp. Fluids* **2012**, *53*, 1855–1866. [CrossRef]
10. Unalmis, O.H.; Clemens, N.T.; Dolling, D.S. Cavity Oscillation Mechanisms in High-Speed Flows. *AIAA J.* **2004**, *42*, 2035–2041. [CrossRef]
11. Rizzetta, D.P. Numerical simulation of supersonic flow over a three-dimensional cavity. *AIAA J.* **1988**, *26*, 799–807. [CrossRef]
12. Chang, K.-S.; Park, S.O. Hybrid RANS/LES Simulation of Deep Cavity Flow. In Proceedings of the 42nd AIAA Aerospace Sciences Meeting and Exhibit, Reno, NV, USA, 5–8 January 2004; American Institute of Aeronautics and Astronautics: Washington, DC, USA, 1996. [CrossRef]
13. Davidson, L.; Peng, S.H. Hybrid LES–RANS Modelling: A One–equation SGS Model Combined with a $k - \omega$ Model for Predicting Recirculating Flows. *Int. J. Numer. Methods Fluids* **2003**, *43*, 1003–1018. [CrossRef]
14. Hamed, A.; Basu, D.; Das, K. Detached Eddy Simulations of Supersonic Flow over Cavity. In Proceedings of the 41st Aerospace Sciences Meeting and Exhibit, Reno, NV, USA, 6–9 January 2003; American Institute of Aeronautics and Astronautics: Washington, DC, USA, 1996. [CrossRef]
15. Tang, Y.; Luo, L.; Zhang, P.; Ma, M. Effect of Rear Wall Inclination on Cavity Acoustic Characteristics at High Mach Numbers. *J. Phys. Conf. Ser.* **2022**, *2252*, 012007. [CrossRef]

16. Jin, X.; Huang, F.; Miao, W.; Cheng, X.; Wang, B. Effects of the boundary-layer thickness at the cavity entrance on rarefied hypersonic flows over a rectangular cavity. *Phys. Fluids* **2021**, *33*, 036116. [CrossRef]
17. Larsson, J.; Davidson, L.; Olsson, M.; Eriksson, L.-E. Aeroacoustic Investigation of an Open Cavity at Low Mach Number. *AIAA J.* **2004**, *42*, 2462–2473. [CrossRef]
18. Lawson, S.J.; Barakos, G.N. Computational Fluid Dynamics Analyses of Flow over Weapons-Bay Geometries. *J. Aircr.* **2010**, *47*, 1605–1623. [CrossRef]
19. Zhang, X.; Chen, X.; Rona, A.; Edwards, J. Attenuation of cavity flow oscillation through leading edge flow control. *J. Sound Vib.* **1999**, *221*, 23–47. [CrossRef]
20. Zhuang, N.; Alvi, F.S.; Alkislar, M.B.; Shih, C. Supersonic Cavity Flows and Their Control. *AIAA J.* **2006**, *44*, 2118–2128. [CrossRef]
21. Vakili, A.D.; Gauthier, C. Control of cavity flow by upstream mass-injection. *J. Aircr.* **1994**, *31*, 169–174. [CrossRef]
22. Luo, K.; Zhe, W.; Xiao, Z.; Fu, S. Improved delayed detached-eddy simulations of sawtooth spoiler control before supersonic cavity. *Int. J. Heat Fluid Flow* **2017**, *63*, 172–189. [CrossRef]
23. Alam, M.; Matsuob, S.; Teramotob, K.; Setoguchib, T.; Kim, H.-D. A new method of controlling cavity-induced pressure oscillations using sub-cavity. *J. Mech. Sci. Technol.* **2007**, *21*, 1398–1407. [CrossRef]
24. Schmit, R.; Semmelmayer, F.; Haverkamp, M.; Grove, J.; Ahmed, A. Examining Passive Flow Control Devices with High Speed Shadowgraph Images around a Mach1.5 Cavity Flow Field. In Proceedings of the 6th AIAA Flow Control Conference, New Orleans, LA, USA, 25–28 June 2012; American Institute of Aeronautics and Astronautics: Washington, DC, USA, 1996. [CrossRef]
25. Danilov, P.; Quackenbush, T. Flow Driven Oscillating Vortex Generators for Control of Cavity Resonance. In Proceedings of the 49th AIAA Aerospace Sciences Meeting Including the New Horizons Forum and Aerospace Exposition, Orlando, FL, USA, 4–7 January 2011; American Institute of Aeronautics and Astronautics: Washington, DC, USA, 1996. [CrossRef]
26. Thangamani, V.; Saddington, A.; Knowles, K. An Investigation of Passive Control Methods for a Large Scale Cavity Model in High Subsonic Flow. In Proceedings of the 19th AIAA/CEAS Aeroacoustics Conference, Berlin, Germany, 24 May 2013; American Institute of Aeronautics and Astronautics: Washington, DC, USA, 1996. [CrossRef]
27. Vikramaditya, N.S.; Kurian, J. Pressure Oscillations from Cavities with Ramp. *AIAA J.* **2009**, *47*, 2974–2984. [CrossRef]
28. Spalart, P.R. Comments on the Feasibility of LES for Wings, and on a Hybrid RANS/LES Approach. In Proceedings of the First AFOSR International Conference on DNS/LES, Ruston, Louisiana, LA, USA, 4–8 August 1997.
29. Baldwin, B.; Lomax, H.T.-l. Approximation and Algebraic Model for Separated Turbulentflows. In Proceedings of the 16th Aerospace Sciences Meeting, Huntsville, AL, USA, 16–18 January 1978; American Institute of Aeronautics and Astronautics: Washington, DC, USA, 1996. [CrossRef]
30. Larcheveque, L.; Sagaut, P.; Lê, T.-H. Large-Eddy Simulations of Flows in Weapon Bays. In Proceedings of the 41st Aerospace Sciences Meeting and Exhibit, Reno, NV, USA, 6–9 January 2003; American Institute of Aeronautics and Astronautics: Washington, DC, USA, 1996. [CrossRef]
31. Rodriquez, G.; Carlos, V.; Marcel, I. Numerical Studies of High-Speed Cavity Flows Using LES, DDES and IDDES. In Proceedings of the 51st AIAA Aerospace Sciences Meeting Including the New Horizons Forum and Aerospace Exposition, Orlando, LA, USA, 1 January 2013.
32. Shyy, W.; Jayaraman, B.; Andersson, A. Modeling of glow discharge-induced fluid dynamics. *J. Appl. Phys.* **2002**, *92*, 6434–6443. [CrossRef]
33. Sinha, N.; Dash, S.; Chidambaram, N.; Findlay, D. A Perspective on the Simulation of Cavity Aeroacoustics. In Proceedings of the 36th AIAA Aerospace Sciences Meeting and Exhibit, Reno, NV, USA, 12–15 January 1998; American Institute of Aeronautics and Astronautics: Reno, NV, USA, 2012. [CrossRef]
34. Bauer, R.C.; Dix, R.E. *Engineering Model of Unsteady Flow in a Cavity*; Arnold Engineering Development Center, US Air Force: Arnold AFB, TN, USA, 1991.